

Double Y-Configuration Multi Active Bridge Converter: A Single Stage Bidirectional AC-DC Converter with Simple Sinusoidal Control

Mafu Zhang, *Student Member, IEEE*, Huanghao Zou, *Student Member, IEEE*, Saleh Farzamkia, *Student Member, IEEE*, Zibo Chen, *Student Member, IEEE*, Chen Chen *Student Member, IEEE*, and Alex Q. Huang, *Fellow, IEEE*

Abstract—This paper proposes a double Y-configuration multi active bridge converter (DYAB) capable of single stage bidirectional AC-DC isolated power conversion with a simple sinusoidal phase shift modulation. Compared to other dual active bridge (DAB) based AC-DC converters, the DYAB achieves power factor correction (PFC) with a simpler control method while maintaining nearly full-range zero-voltage switching (ZVS) and relatively low circulating current, resulting in high efficiency. The paper details the equivalent model and modulation method. A steady-state analysis tool based on the fast fourier transform (FFT) is developed to calculate the ZVS range, PFC performance, and loss breakdown. A 2.66kW hardware test demonstrating an efficiency of 97.14% is implemented to verify the proposed circuit and the steady state model.

Index Terms—AC-DC converter, bidirectional, dual active bridge converter, Y-configuration active bridge, isolation, phase shift control, single stage conversion, three phase, YAB, zero voltage switching.

I. INTRODUCTION

IN recent years, isolated AC-DC converters have gained significant attentions due to their wide applications in solid-state transformers, EV fast charging, PV micro-inverters, and battery energy storage systems. Among the various isolated AC-DC bidirectional topologies, the single-stage AC-DC DAB is widely adopted due to its zero voltage switching (ZVS) performance and high efficiency. The principle of the AC-DC DAB is that the AC voltage is first rectified to a 120Hz half-sine, and then the DAB converter smooths it to a constant DC. With a large DC-link capacitor on the DC side, the 120 Hz current ripple is filtered, which results in a constant DC current. The sine to half-sine unfolding operation can be achieved with either an AC switch half-bridges or an active unfolding bridge stage.

In [1], an AC-DC DAB with an active unfolding bridge is presented. The author discusses the optimal ZVS modulation

method considering different ZVS criteria. This method effectively achieves full-range ZVS and a peak efficiency of 96.3%. However, the relatively high circulating current necessary to enforce the ZVS leads to higher conduction loss. Additionally, the need to consider different switching modes makes this method complex.

In [2], [3], a variable frequency with single switching mode method is proposed. The PFC is maintained with double phase shift and varying switching frequency (DPS-VF). The switching frequency increases significantly when the AC side voltage approaches the zero-crossing in order to maintain the ZVS. A similar method is adopted in [4], where an efficiency optimization considering semiconductor and magnetic component losses is implemented. An efficiency of 96.6% is achieved with switching frequencies ranging from 50 kHz to 300 kHz. The efficiency is not significantly increased compared to fixed frequency methods in [1], [5]. This might be due to the fact that true full range ZVS is actually impossible to achieve in the hardware since partial ZVS or hard switching is inevitable near the AC zero-crossing. Therefore high switching frequency will result in an increased switching loss. Additionally, high switching frequency leads to higher transformer core loss compared to fixed frequency methods. Thus, it remains unclear whether variable frequency control truly enhances the efficiency of an AC-DC DAB. It requires a more thorough modeling of partial ZVS loss and core loss under asymmetric leakage inductance.

Series resonant DAB (SR-DAB) are discussed in [6], [7]. With the same DPS-VF modulation, the efficiency is increased from 96.6% to 97.2%. With the same power transferred within one switching period, the rising and falling edges of the current are more leading compared to a non-resonant DAB, therefore the half bridge switching current is decreased. The disadvantage is that the ZVS is harder to achieve than a DAB due to a lower turn on current, while the advantage is that the turn off loss and the circulating current are effectively decreased. Variable frequency control is more effective here because it solves the trade off between the ZVS difficulty and loss minimization. In conclusion, frequency modulation is more suitable for a SR-DAB than a DAB.

The aforementioned methods all share a common flaw: it requires the implementation of an off-line or on-line modulation solver. Not only the look-up table might become

This work was supported in part by ONR GRANT 00014-21-1-2124. DCN # 0543-1987-24.

Mafu Zhang, Huanghao Zou, Zibo Chen, Saleh Farzamkia, Chen Chen and Alex Q. Huang are with the Semiconductor Power Electronics Center at the University of Texas at Austin, Austin, TX 78712 USA (e-mail: mafuzhang@utexas.edu; hzou@utexas.edu; zibochen@utexas.edu; farzam@utexas.edu; chenchen@utexas.edu; aqhuang@utexas.edu).

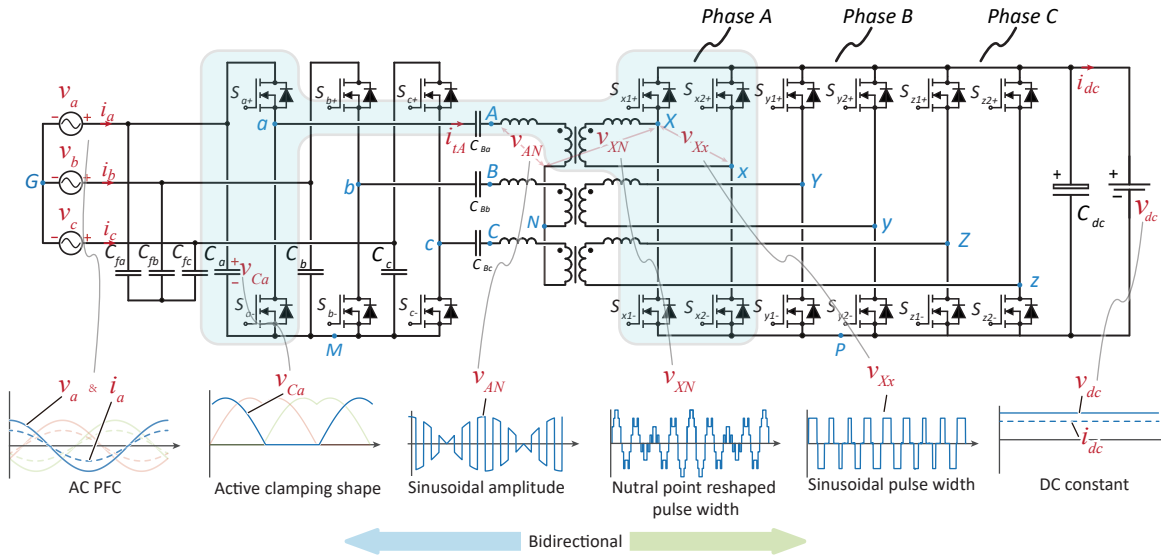


Fig. 1. Proposed Y-configuration Dual Active Bridge converter

computationally challenging, it makes close loop power flow or voltage control more difficult to achieve.

To address this problem, simpler modulation methods are widely studied. A sinusoidal duty cycle method for half-bridge AC-DC DAB is discussed in [8], where the author apply a sinusoidal duty cycle to the DC side half-bridge while maintain a constant phase shift between the AC side and DC side. Under DC-AC operation, significant 3rd and 5th harmonic distortion in the AC voltage is observed. To solve this problem, the author introduces third harmonic injection to the DC side duty cycle, reducing the THD from 9.8% to 2.3% and achieving a peak efficiency of 96.8%. While effective, this method still lacks simplicity due to the need for online calculation of the injected harmonic. Sinusoidal phase shift methods are explored in [9], [10], where similar power factor distortion problem was noticed. This suggests that, unlike most DC-AC converters, DAB cannot maintain PFC with simple sinusoidal modulation on the DC side.

In [11], a novel high-frequency link Y-configuration on the transformer winding was proposed, effectively solving the power factor distortion problem under DC side sinusoidal space vector modulation. However, this topology has relative high circulating current at zero-crossing, which increases the conduction loss.

In this paper, a novel double Y-configuration multi active bridge (DYAB) converter for three-phase AC-DC application is proposed. By combining the merits of the AC-DC DAB and the Y-configuration circuit structure in [11], the DYAB overcomes the complex modulation problems of traditional AC-DC DAB. It achieves good PFC with simple sinusoidal phase shift modulation and maintains near-full-range ZVS for different output powers. An experimental test achieved a efficiency of 97.14%. A fast fourier transform (FFT) based analysis tool is developed for both the AC-DC DAB and the proposed DYAB, and is available on GitHub [12].

This paper is organized as follows: Section II introduces the proposed topology and derives the equivalent circuit model.

Section III details the modulation methods and explains how to decouple the three-phase system. Section IV analyzes the steady-state model and implements it with the FFT algorithm. Based on this, system power, ZVS performance, loss breakdown, and efficiency calculations are conducted. Finally, the hardware test results are presented in Section V.

II. TOPOLOGY AND EQUIVALENT CIRCUIT

A. Introduction to the topology

The proposed DYAB converter is shown in Fig.1. The blue shielded part is a DAB structure responsible for the power conversion of phase A. Three of these structures are coupled together through two Y-configurations: a low frequency (LF) Y-configuration on the AC side half-bridges (HBs) and a high-frequency (HF) Y-configuration on the winding of high-frequency transformer (HFT). For clarity, the AC side half-bridges are referred to as HB-a, HB-b, and HB-c, while the DC side half-bridges are referred to as HB-x1, HB-x2, HB-y1, HB-y2, HB-z1, and HB-z2 etc.

The positive terminals of HB-a, HB-b, and HB-c are directly connected to the three phase grid, and the negative terminals are connected together to form a neutral point M. The neutral point M needs to be floating from the grid neutral G. Blocking capacitors C_{Ba} , C_{Bb} , and C_{Bc} are placed between the AC side half-bridges and the HFT to block the grid frequency component. As shown in the waveform examples in Fig.1, considering phase A as an example, the grid side demonstrates sinusoidal voltage v_a and current i_a with high power factor (PF), while the input capacitor voltage v_{Ca} appears as a camel hump shape. Then, with a simple synchronous 50% duty cycle switching on HB-a, HB-b, and HB-c, a high-frequency pulse v_{AN} with a sinusoidal envelope is generated on the HFT's AC side winding.

The DC side 6 HBs share the same dc link. For phase A, HB-x1 and HB-x2 do a sinusoidal phase shift to generated a sinusoidal pulse width v_{Xx} . Due to the floating neutral point N, v_{Xx} is reshaped by the other two phase into v_{XN} , which

is the effective voltage applied on the right side of leakage inductance. With a constant phase shift between v_{XN} and v_{AN} , a high PF power flow is achieved.

B. Three phase equivalent circuit

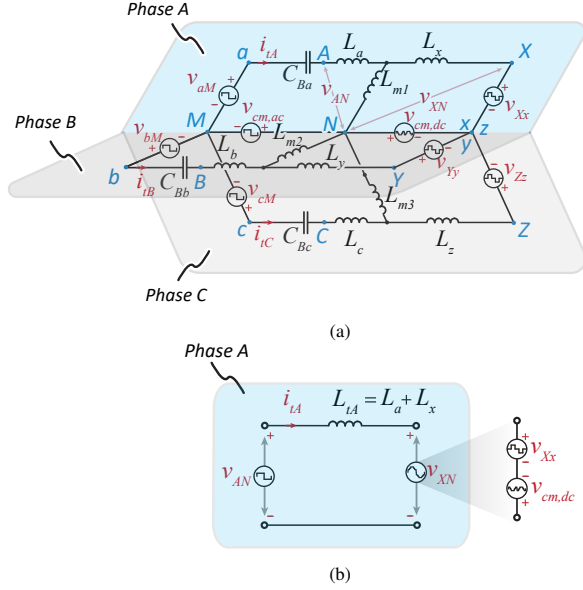


Fig. 2. (a) The three phase HF equivalent circuit and (b) the decoupled single phase HF equivalent circuit.

The three-phase high-frequency (HF) equivalent circuit is illustrated in Fig.2a. Considering phase A (blue shielded part) as an example, the AC side HF voltage source is the voltage on switch S_{a-} , and the DC side HF voltage source is the voltage across switching node X and x . L_a and L_x are the transformer leakage inductances on the AC and DC sides, respectively. L_m is the magnetizing inductance. Phases A, B, and C are coupled together through nodes M , N , and (xyz) . To simplify the analysis, the three-phase equivalent circuit can be decoupled into the single-phase equivalent circuit shown in Fig.2b. The derivation of v_{AN} and v_{XN} , which is detailed in Section.III, is required for this decoupling.

III. MODULATION METHOD

A. Start-up with active clamping

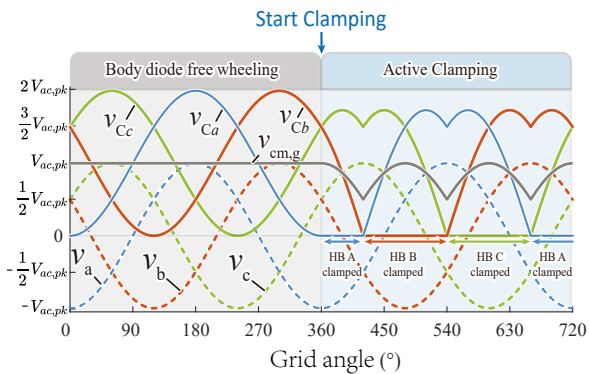


Fig. 3. Start up the DYAB with active clamping on the AC side HBs.

the HB- a HB- b HB- c form the famous three phase Y-configuration half bridge structure [13]. Before starting, all switches are off. The body diodes and the input capacitors forms a freewheeling circuit, with which a constant common mode (CM) voltage $v_{cm,g}$ is established on C_a C_b C_c , which keeps the HB input voltage v_{Ca} v_{Cb} and v_{Cc} positive (c.f., Fig.3).

An active clamping method discussed in [14] is further employed here. Starting with phase A, when the capacitor voltage v_{Ca} reaches zero, the top and bottom switches on HB- a are both turned on to clamp v_{Ca} at zero. After 60° , when v_{Cb} decreases to zero, clamping on HB- a is released, and HB- b begins clamping. After another 120° , the clamping shifts from HB- b to HB- c and continues. In this way, the common-mode voltage $v_{cm,g}$ changes from a constant DC to a 180Hz varying DC, and v_{Ca} , v_{Cb} , and v_{Cc} demonstrate a camel hump shape. Meanwhile, the AC phase voltages as the differential-mode (DM) components still maintain their sinusoidal shape.

B. AC side modulation

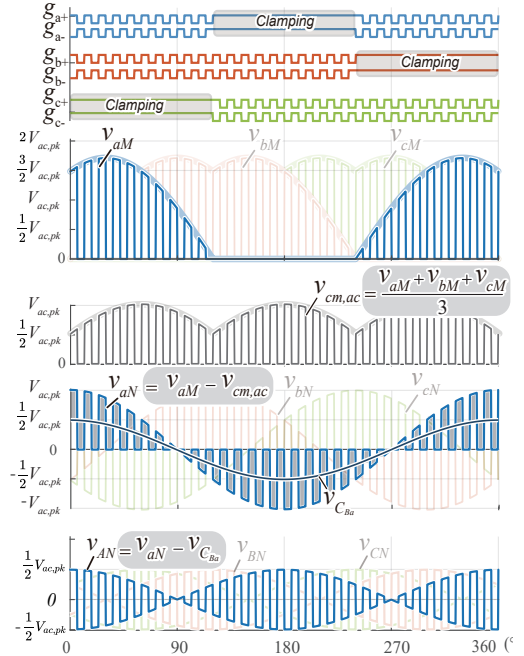


Fig. 4. Modulation on the AC side and the generated switching waveforms. From top to bottom: gate signals, switching node voltages with respect to M , AC side HF common-mode component $v_{cm,ac}$ (i.e., v_{NM}), switching node voltage with respect to N , and the final effective HF pulse applied to the HFT winding.

As shown in Fig.4, for every 120° , one HB is clamped while the remaining two operate with synchronous 50% duty cycle switching. The generated v_{aM} is a unipolar pulse with an upper envelope equal to the camel hump v_{Ca} . Considering the loop M - a - N and applying KVL:

$$v_{AN} = v_{aM} - v_{C_{Ba}} - v_{cm,ac}. \quad (1)$$

Here, $v_{cm,ac}$, i.e., v_{NM} , is the HF CM component generated by v_{AM} , v_{BM} , and v_{CM} , and can be calculated as:

$$v_{cm,ac} = \frac{v_{aM} + v_{bM} + v_{cM}}{3}. \quad (2)$$

As shown in Fig.4, $v_{cm,ac}$ has an envelope equal to the 180Hz LF CM $v_{cm,g}$. By subtracting it from v_{aM} , the HF DM v_{aN} is obtained. The blocking capacitor C_{Ba} blocks the 60Hz component in v_{aM} , resulting in the final effective HF AC voltage v_{AN} applied to the transformer winding, which is decoupled from the other two phases. v_{BN} and v_{CN} can be obtained similarly.

C. DC side modulation

As introduced in Section I, the DC side modulation is a simple sinusoidal modulation. The principle is to keep the voltage-time product equal for the switching pulses of the AC side and the DC side, i.e., keep the areas $A_{DC} = A_{AC}$ (cf. Fig. 6). Assuming the grid voltages are:

$$\begin{aligned} v_a &= V_g \cdot \cos(2\pi f_g t), \\ v_b &= V_g \cdot \cos(2\pi f_g t - \frac{2\pi}{3}), \\ v_c &= V_g \cdot \cos(2\pi f_g t + \frac{2\pi}{3}). \end{aligned} \quad (3)$$

Then the DC side inner phase shifts are:

$$\begin{aligned} d_X &= \frac{v_a}{2V_{DC}} \cdot \frac{T_{sw}}{2}, \\ d_Y &= \frac{v_b}{2V_{DC}} \cdot \frac{T_{sw}}{2}, \\ d_Z &= \frac{v_c}{2V_{DC}} \cdot \frac{T_{sw}}{2}. \end{aligned} \quad (4)$$

In this way, the sinusoidal pulse width modulated v_{Xx} , v_{Yy} , and v_{Zz} are generated (cf. Fig. 5). However, unlike an ordinary DAB, these are not the effective voltages directly applied on the leakage inductance; a common-mode component $v_{cm,dc}$ among them causes a major difference:

$$v_{cm,dc} = \frac{v_{Xx} + v_{Yy} + v_{Zz}}{3}, \quad (5)$$

By subtracting $v_{cm,dc}$ from them, the effective DC side pulses v_{XN} , v_{YN} , and v_{ZN} are obtained:

$$\begin{aligned} v_{XN} &= v_{Xx} - v_{cm,dc}, \\ v_{YN} &= v_{Yy} - v_{cm,dc}, \\ v_{ZN} &= v_{Zz} - v_{cm,dc}. \end{aligned} \quad (6)$$

With the derived AC side effective pulses v_{AN} , v_{BN} , v_{CN} and DC side effective pulses v_{XN} , v_{YN} , v_{ZN} , the three-phase equivalent model in Fig. 2a is decoupled into three single-phase models. Assuming the transformer magnetizing inductance is infinitely large, the final equivalent circuit is simplified into Fig. 2b.

For phase A, the control logic is illustrated in Fig. 6. The DC side pulse width d_X is a dependent variable determined by the grid voltage v_a , while φ , the phase shift between v_{AN} and v_{XN} , is the main variable that controls the system power. Three phases share the same φ , and it remains constant for a given power. It changes only when the output power (voltage source load) or output voltage (resistive load) needs to be adjusted. Compared to the AC-DC DAB, which requires off-line calculation for at least two variables to control power and maintain PFC, the single-variable control of the DYAB is much simpler.

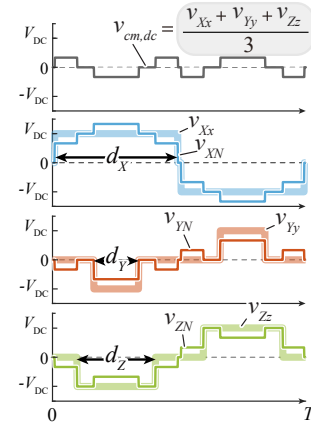


Fig. 5. DC side modulation method: v_{Xx} , v_{Yy} , and v_{Zz} are the voltages across the switching nodes of the full bridges. They contain a common-mode component $v_{cm,dc}$. By subtracting this common-mode component, the decoupled effective pulses v_{XN} , v_{YN} , and v_{ZN} are obtained.

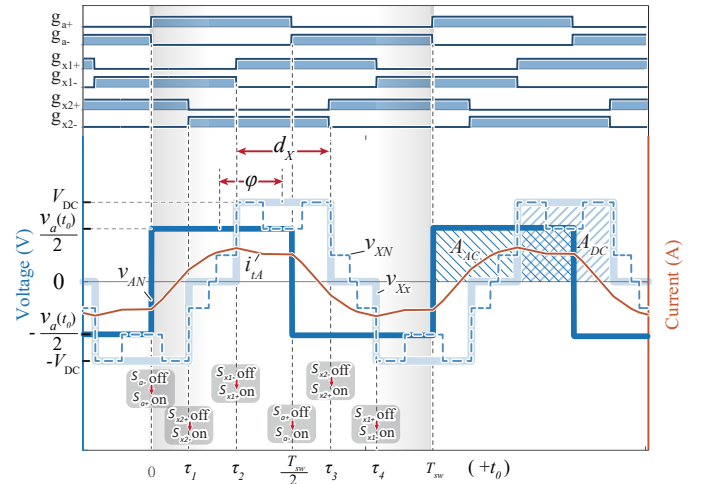


Fig. 6. Phase shift modulation of Phase A at time instant t_0 . The AC side is constant 50% duty cycle square pulse, with a amplitude following grid voltage $\frac{V_g}{2}$. The DC side is a three voltage level waveform with constant amplitude of V_{DC} , while its duty cycle is sinusoidal modulated according to the principle $A_{DC} = A_{AC}$.

IV. STEADY STATE MODELING

Steady-state modeling of DAB type converters using time-domain methods is troublesome due to the multiple switching modes. In contrast, frequency-domain methods can greatly simplify the process as switching modes no longer need to be considered. Therefore, a straightforward FFT based modeling approach proposed in [15] is adopted here to analyze the system.

In the following derivation, the system parameters listed in Table.I are considered. All waveform variables in bold font are discrete arrays.

A. Calculation of inductor current i_{lA}

Obtaining the leakage inductor current waveform is the first step. This waveform is essential for calculating device switching currents, conduction currents, transformer currents, and system instantaneous power.

TABLE I. System parameters

Parameters	Description	Value
SW	Selected MOSFET	C3M0021120K
V_{DC}	DC voltage	200V
V_{LL}	Grid line-line voltage	480V _{rms}
f_g	Grid frequency	60Hz
N_t	HFT Turns ratio	1:1
L_μ	HFT leakage inductance	4.7μH
L_e	Extra inductance	14.6μH
C_B	Blocking capacitance	4.5μF
P_{ave}	System total power	-4.37kW~4.37kW
φ	Phase shift	-0.5T _{sw} ~0.5T _{sw}
f_{sw}	Switching frequency	100kHz

One switching period is taken as the analysis object, which is the grey-shaded area in Fig. 6 starting from t_0 and ending at $t_0 + T_{sw}$. The following conditions are assumed within this analyzed period:

1. The grid voltage v_a is constant.
2. The blocking capacitor voltage $v_{C_{Ba}}$ is constant.
3. The DC link capacitor voltage is constant.
4. Switching transients are ignored.

The FFT model is numerical, in which all waveforms are sampled into arrays of length N_s (N_s must be even). The derivation starts with obtaining all gate signals g_{a+} , g_{x1+} , and g_{x2+} .

Using g_{a+} as the reference:

$$\mathbf{g}_{a+} = \left[\underbrace{1, 1, \dots, 1}_{N_s/2}, \underbrace{0, 0, \dots, 0}_{N_s/2} \right]; \quad (7)$$

The others can be obtained by circularly shifting \mathbf{g}_{a+} :

for $n \in \{1, 2, \dots, N_s\}$,

$$\begin{cases} \tau_1 = \frac{T_{sw}}{4} + \varphi - \frac{d_x}{2}, \\ k_1 = \text{mod} \left(\lfloor n - N_s \frac{\tau_1}{T_{sw}} \rfloor, N_s \right), \\ \mathbf{g}_{x1+}(n) = \mathbf{g}_{a+}(k_1) \end{cases} \quad (8)$$

$$\begin{cases} \tau_2 = \frac{T_{sw}}{4} + \varphi + \frac{d_x}{2}, \\ k_2 = \text{mod} \left(\lfloor n - N_s \frac{\tau_2}{T_{sw}} \rfloor, N_s \right), \\ \mathbf{g}_{x2+}(n) = \mathbf{g}_{a+}(k_2) \end{cases} \quad (9)$$

Then the voltage pulses can be obtained with:

$$v_{AN} = v_a(t_0) \cdot \mathbf{g}_{a+} \quad (10)$$

$$v_{XN} = V_{DC} \cdot (\mathbf{g}_{x1+} - \mathbf{g}_{x2+}) \quad (11)$$

Therefore, the voltage applied on the leakage inductance L_{ax} is:

$$\mathbf{v}_L = \mathbf{v}_{AN} - \mathbf{v}_{XN} \quad (12)$$

Applying FFT to \mathbf{v}_L to obtain the frequency domain \mathbf{V}_L :

$$\mathbf{V}_L = \mathcal{F}(\mathbf{v}_L) \quad (13)$$

The \mathbf{V}_L is a complex array with a length of N_s , where the n^{th} component $\mathbf{V}_L(n)$ represents the magnitude and phase of the

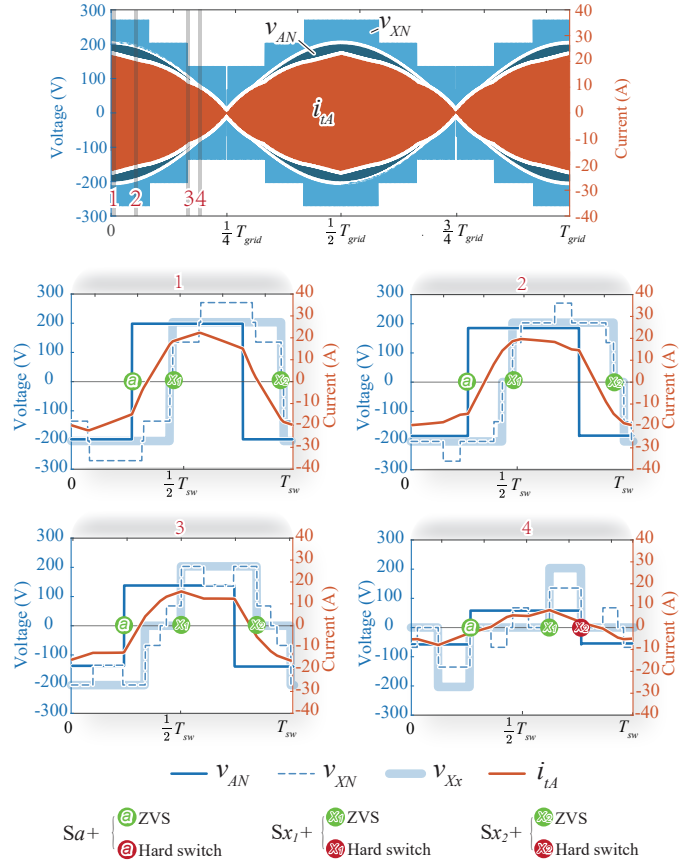


Fig. 7. Calculated inductor current i_{L_A} , with a system parameter of $V_{LL} = 480V_{rms}$, $V_{DC} = 200V$, $L_{L_A} = L_{L_B} = L_{L_C} = 20.3\mu H$, $\varphi = 0.18T_{sw}$, $P = 4kW$. Switching period instance 1,2,3,4 at different grid angle are zoomed in. The ZVS and hard switching are indicated in the zoomed-in figures, respectively with green dots, and red dots.

n^{th} harmonic. According to [15], the components from $\frac{N_s}{2}^{\text{th}}$ to N_s^{th} in \mathbf{V}_L must be set to zero to avoid the Gibbs phenomenon, i.e., resonance at switching instants. Additionally, the first component is also set to zero because the DC component in i_{L_A} is zero. Therefore, the frequency domain voltage becomes:

$$\tilde{\mathbf{V}}_L = [0 + 0j, \mathbf{V}_L(2), \mathbf{V}_L(3), \dots, \mathbf{V}_L(\frac{N_s}{2}), \underbrace{0 + 0j, \dots, 0 + 0j}_{N_s/2}]. \quad (14)$$

The frequency domain inductor current can be calculated as:

$$\tilde{\mathbf{I}}_{L_A} = \frac{\tilde{\mathbf{V}}_L}{j\omega L_{L_A}} \quad (15)$$

where ω is the frequency of each component in $\tilde{\mathbf{V}}_L$:

$$\omega = 2\pi f_{sw} \cdot [0, 1, 2, \dots, N_s]. \quad (16)$$

Then the inductor current for one switching period can be calculated using the Inverse FFT:

$$\mathbf{i}_{L_A} = \mathcal{F}^{-1}(\tilde{\mathbf{I}}_{L_A}) \quad (17)$$

By repeating this calculation for

$$t_0 \in [1, 2, \dots, 360] \frac{T_{grid}}{360}, \quad (18)$$

a whole line period inductor current result is obtained. Phase B and phase C can be obtained similarly. In actual implementation in MATLAB, this is achieved through vectorization, which the reader can refer to [12]. This main calculation part can be implemented with a few dozens of lines in MATLAB, which saves significant effort compared to the complex time-domain multi-mode methods discussed in [1], [16]–[19].

As shown in Fig. 7, the v_{AN} , v_{XN} , and i_{tA} are calculated for a whole grid period. With a positive $\varphi = 0.18T_{sw}$, i.e., v_{AN} leads v_{XN} , the average power flows from the AC side to the DC side. The system operates in rectifier mode.

Zoomed-in figures 1, 2, 3, and 4 show the waveforms of effective voltages and inductor current, indicating the ZVS status of the three top switches S_{a+} , S_{x1+} , and S_{x2+} . The green dot indicates ZVS, while the red dot indicates hard switching. It can be observed that in figures 1, 2, and 3, all switches achieve ZVS. Only in figure 4, where the grid voltage is close to zero crossing, does HB-x2 lose ZVS, while the other two HBs still maintain ZVS.

B. Calculation of system power

There exist three power quantities, the first is the instant power, which is the product of instant current and instant voltage:

$$\begin{aligned} p_a &= v_{AN}i_{tA} \\ p_b &= v_{BN}i_{tB} \\ p_c &= v_{CN}i_{tC} \\ p &= p_a + p_b + p_c. \end{aligned} \quad (19)$$

The second is the local averaged power with respect to a switching period. For an ideal system with a power factor of 1.0, it is constant.

$$p_{local} = \sum_{n=1}^{N_s} p. \quad (20)$$

The third is the averaged power with respect to a grid period.

$$p_{ave} = \frac{1}{T_{grid}} \int_0^{T_{grid}} p_{local} dt \quad (21)$$

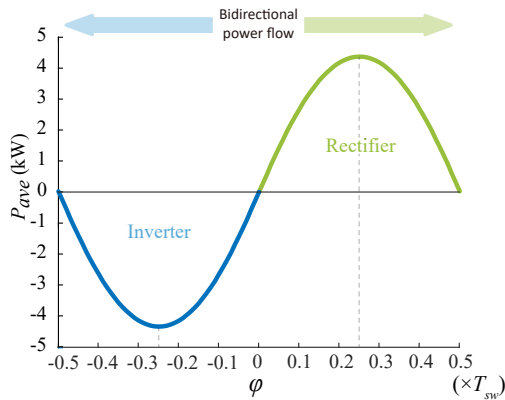


Fig. 8. System total power and its relationship with the control variable φ .

In YAB, P_{ave} is controlled solely by the phase shift φ . As shown in Fig. 8, when $\varphi > 0$, the power is positive, which means power flows from the AC side to the DC side.

Conversely, when $\varphi < 0$, power flows from the DC side to the AC side. For $\varphi \in [0, 0.25T_{sw}]$, the power increases with increasing φ . When φ exceeds $0.25T_{sw}$, the power decreases with increasing φ . This behavior is exactly the same as in a DC-DC DAB. Due to page limit, detail comparison on the PFC between YAB and AC-DC DAB is omitted here, and will be add to the final paper.

C. ZVS analysis

The criterion for determining ZVS is that the device current must be negative at the instant of turning on, i.e., the current must be flowing through the body diode so that the turn-on voltage is zero. According to Fig. 6, the turn-on current of each device can be derived as follows:

$$\begin{aligned} -t = 0: S_{a+} \text{ turns on. } i_{sw,a+} &= i_{tA}|_{n=0}. \\ -t = \tau_2: S_{x1+} \text{ turns on. } i_{sw,x1+} &= -i_{tA}|_{n=\lfloor \frac{\tau_2}{T_{sw}} N_s \rfloor}. \\ -t = \tau_3: S_{x2+} \text{ turns on. } i_{sw,x2+} &= i_{tA}|_{n=\lfloor \frac{\tau_3}{T_{sw}} N_s \rfloor}. \end{aligned}$$

Due to symmetry, the switching status of the bottom switches is the same as the top switches: $i_{sw,a-} = i_{sw,a+}$, $i_{sw,x1-} = i_{sw,x1+}$, $i_{sw,x2-} = i_{sw,x2+}$. Therefore, only the turn-on currents of the top switches need to be investigated. Moreover, since HB-x1 and HB-x2 perform sinusoidal phase shifts within a grid period, their turn-on currents are symmetrical within the grid period. Therefore, this paper only investigates the results for S_{a+} and S_{x1+} in the following text.

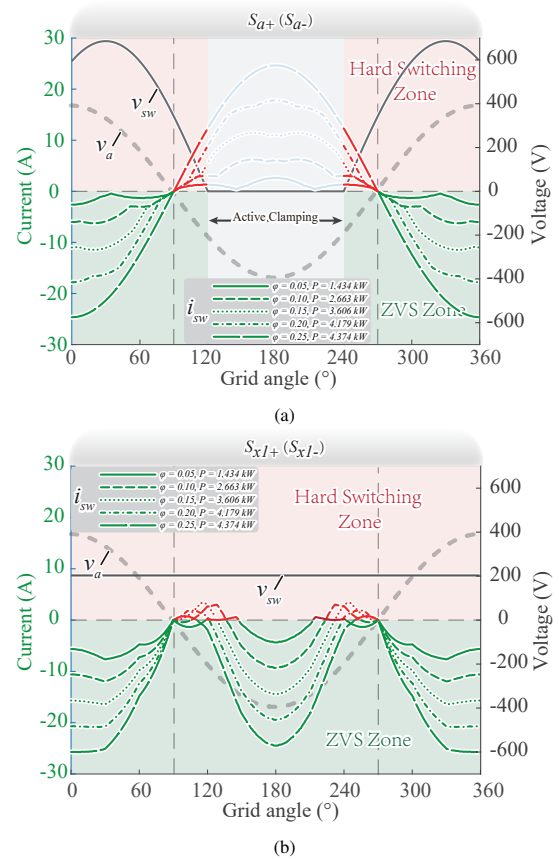


Fig. 9. Turn on current of (a) S_{a+} (Same for S_{a-}), (b) S_{x1+} (same for S_{x1-}) at different power level, i.e., different φ .

The turn-on currents of S_{a+} and S_{x1+} within a grid period under different output power ($\varphi = 0.05 \sim 0.25 T_{sw}$) are shown

in Fig. 9. Negative current in the green zone indicates ZVS, while positive current in the red zone indicates hard switching. The black line represents the device switching voltage. The grid voltage, shown as a grey dashed line, helps the reader locate where hard switching occurs within one grid period.

The turn-on current of S_{a+} in Fig. 9a shows that it maintains ZVS from 0° to 90° and from 270° to 360° , where the grid voltage is positive. Hard switching occurs from 90° to 120° and from 240° to 270° . HB- a is clamped from 120° to 240° , during which there is no switching loss. Generally, the higher the output power, the higher the switching current, but the ZVS locations within a grid period remain the same for different output powers (or φ).

The turn-on current of S_{x1+} is shown in Fig. 9b. For most of the grid period, it maintains ZVS. The hard switching distributions vary slightly with different power levels but always last for a short duration and are located near the zero crossing. Consequently, the hard switching current is low, resulting in low switching loss.

D. Loss model and efficiency estimation

The major component losses are calculated for different power levels, and the system theoretical efficiency is obtained accordingly.

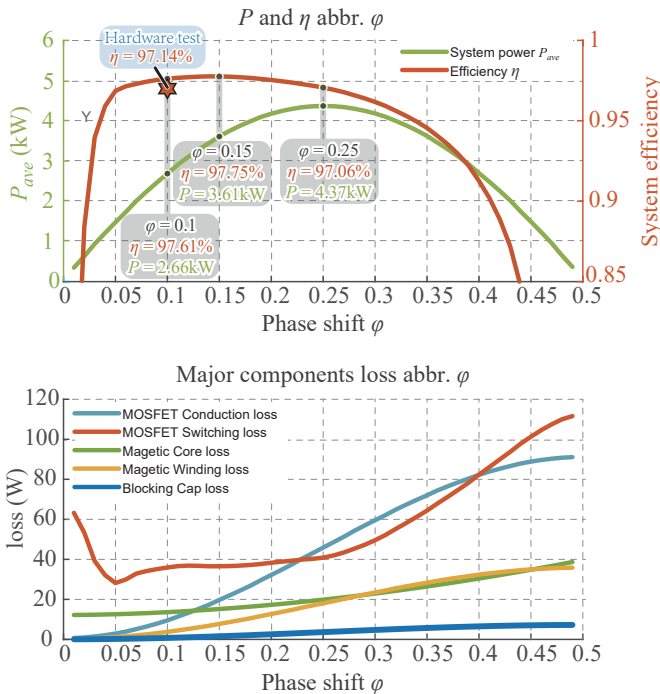


Fig. 10. The system power P_{ave} , efficiency η , and major loss components abbr. phase shift φ .

The results are shown in Fig. 10. The theoretical peak efficiency of 97.75% is obtained when $\varphi = 0.15$. The efficiency at peak power is 97.06%. An experimental result of 97.14% was obtained at $\varphi = 0.1$, where the theoretical efficiency is 97.61%. This 0.47% error could be the partial ZVS loss and other filter component losses.

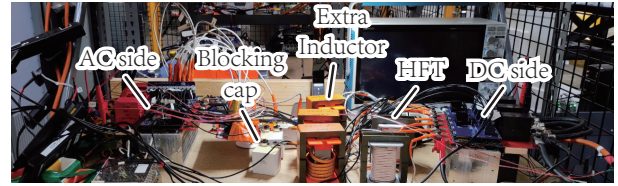


Fig. 11. The experiment set up of the proposed YAB.

V. HARDWARE TEST

A hardware test in rectifier mode ($\varphi = 0.1T_{sw}$) with a resistive load ($R_L = 15.6\Omega$), and other parameters as listed in Table I, was conducted in the SPEC lab at UT Austin (cf. Fig. 11). The waveform of phase A is shown in Fig. 12. From top to bottom, the respective waveforms are: $v_{LL,ab}$, the line-to-line voltage between phase A and phase B; v_{Ca} , the phase A input capacitor voltage with active clamping shape; i_a , the grid input current; v_{Sa-} , the voltage on switch S_{a-} ; v_{Sx1-} , the voltage on switch S_{x1-} ; $i_{tA,p}$ and $i_{tA,s}$, the leakage inductor currents on the primary and secondary sides; and v_{DC} , the DC output voltage.

The reader can notice that the grid current i_a is leading to the input capacitor voltage v_{Ca} . This is because the filter capacitor is in paralleled with the converter, of which the current is 90° leading v_{Ca} , which add to the PFC current to make the i_a leading. This is common for rectifier with input filter, and can be solved with better input filter design [1].

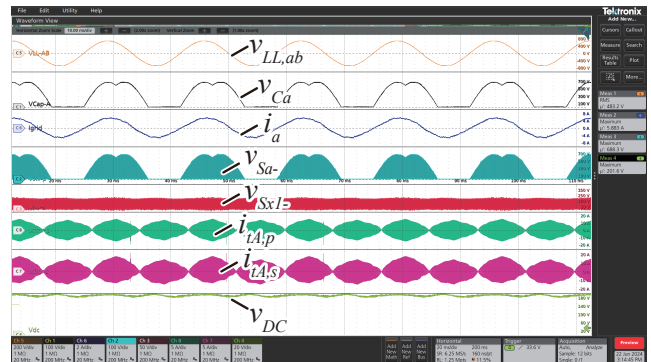


Fig. 12. Hardware test results.

In Fig. 13, the switch voltages v_{Sa-} , v_{Sx1-} , and inductor currents $i_{tA,p}$ and $i_{tA,s}$ are zoomed in to investigate the ZVS status. $i_{tA,p}$ and $i_{tA,s}$ are measured such that positive values indicate current flowing out from the HB switching node. The rising edges of v_{Sa-} and v_{Sx1-} corresponds to the turn on of S_{a+} and S_{x1+} . Therefore if measured current is negative at this instant, the corresponding HB achieve ZVS. It is clear that ZVS is achieved for both HB- a and HB- $x1$ at 0° , 20° , 50° , and 70° . Hard switching occurs at 110° . From 130° to 180° , HB- a is clamped while HB- $x1$ maintains ZVS. This test result perfectly aligns with the modeling results in Fig. 9.

VI. CONCLUSION

This paper proposed a new double Y-configuration multi active bridge converter (DYAB), which eliminates the complex control problem that exists in traditional AC-DC DAB

converters while achieving higher efficiency. The equivalent circuit model and the method to decouple the three phases are detailed. A steady state analyzer tool box based on FFT is developed, which not only facilitates the analysis of the proposed YAB, but also can be easily modified for other types of AC-DC DAB converter. The experimental tested efficiency is 97.14%, while the calculated peak efficiency is 97.75%. In the future, a multi-objective optimization effort will be carried to improve the hardware to reach higher efficiency.

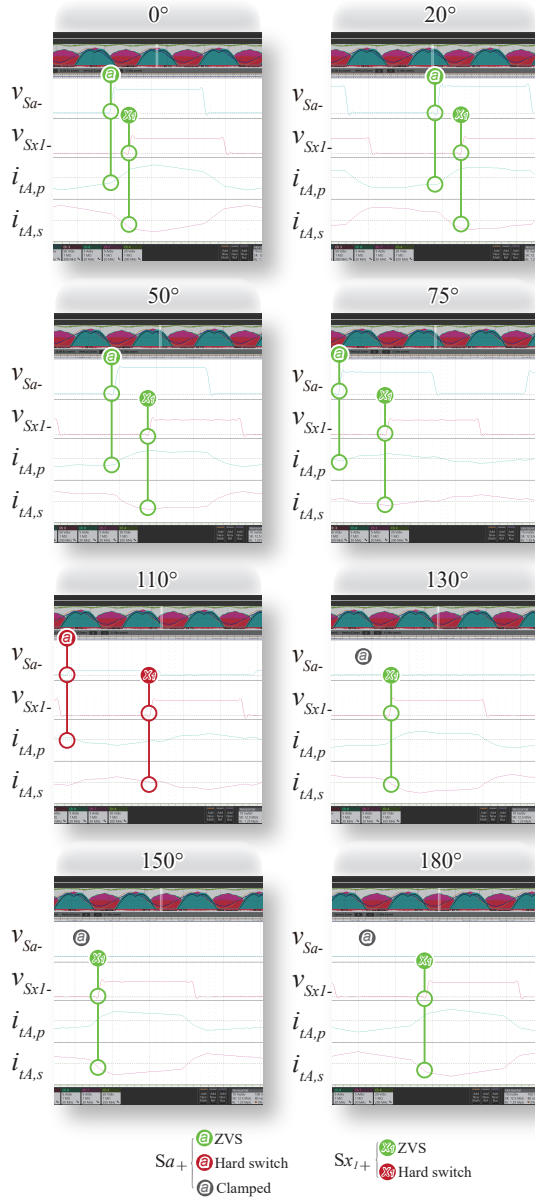
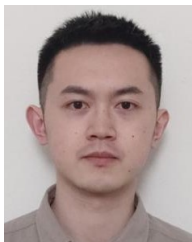


Fig. 13. Zoomed-in figure at different angle from 0° to 180° to verify the theoretical ZVS results in Fig.9.

REFERENCES

- [1] J. Everts, F. Krismer, J. Van den Keybus, J. Driesen, and J. W. Kolar, "Optimal zvs modulation of single-phase single-stage bidirectional dab ac-dc converters," *IEEE Transactions on Power Electronics*, vol. 29, DOI 10.1109/TPEL.2013.2292026, no. 8, pp. 3954–3970, 2014.
- [2] F. Jauch and J. Biela, "Combined phase-shift and frequency modulation of a dual-active-bridge ac-dc converter with pfc," *IEEE Transactions on Power Electronics*, vol. 31, DOI 10.1109/TPEL.2016.2515850, no. 12, pp. 8387–8397, 2016.
- [3] F. Jauch and J. Biela, "Single-phase single-stage bidirectional isolated zvs ac-dc converter with pfc," in *2012 15th International Power Electronics and Motion Control Conference (EPE/PEMC)*, DOI 10.1109/EPEPEMC.2012.6397479, pp. LS5d.1–1–LS5d.1–8, 2012.
- [4] T. Chen, R. Yu, and A. Q. Huang, "Variable-switching-frequency single-stage bidirectional gan ac-dc converter for the grid-tied battery energy storage system," *IEEE Transactions on Industrial Electronics*, vol. 69, DOI 10.1109/TIE.2021.3120483, no. 11, pp. 10776–10786, 2022.
- [5] J. Lu, K. Bai, A. R. Taylor, G. Liu, A. Brown, P. M. Johnson, and M. McAmmond, "A modular-designed three-phase high-efficiency high-power-density ev battery charger using dual/triple-phase-shift control," *IEEE Transactions on Power Electronics*, vol. 33, DOI 10.1109/TPEL.2017.2769661, no. 9, pp. 8091–8100, 2018.
- [6] T. Chen, R. Yu, and A. Q. Huang, "A bidirectional isolated dual-phase-shift variable-frequency series resonant dual-active-bridge gan ac dc converter," *IEEE Transactions on Industrial Electronics*, vol. 70, DOI 10.1109/TIE.2022.3181349, no. 4, pp. 3315–3325, 2023.
- [7] H. Zou, R. Yu, R. Anand, J. Tong, and A. Q. Huang, "A gan variable-frequency series resonant dual-active-bridge bidirectional ac-dc converter for battery energy storage system," in *2023 IEEE Applied Power Electronics Conference and Exposition (APEC)*, DOI 10.1109/APEC43580.2023.10131248, pp. 150–157, 2023.
- [8] T.-T. Le, J. Lee, and S. Choi, "Single-stage totem-pole ac-dc converter based on boost half-bridge structure for battery chargers," *IEEE Transactions on Power Electronics*, vol. 39, DOI 10.1109/TPEL.2023.3323946, no. 1, pp. 1060–1073, 2024.
- [9] S. Zengin and M. Boztepe, "A novel current modulation method to eliminate low-frequency harmonics in single-stage dual active bridge ac-dc converter," *IEEE Transactions on Industrial Electronics*, vol. 67, DOI 10.1109/TIE.2019.2898597, no. 2, pp. 1048–1058, 2020.
- [10] M. Zhang, H. Zou, S. Farzamkia, Z. Chen, and A. Q. Huang, "New single-stage single-phase isolated bidirectional ac-dc pfc converter," in *2024 IEEE Applied Power Electronics Conference and Exposition (APEC)*, DOI 10.1109/APEC48139.2024.10509329, pp. 1962–1967, 2024.
- [11] D. Menzi, F. Krismer, T. Ohno, J. Huber, J. Kolar, and J. Everts, "Novel bidirectional single-stage isolated three-phase buck-boost pfc rectifier system," in *2023 IEEE Applied Power Electronics Conference and Exposition (APEC)*, DOI 10.1109/APEC43580.2023.10131553, pp. 1936–1944, 2023.
- [12] M. Zhang, "Github," 2024. [Online]. Available: <https://github.com/MafuZhang/YAB-Analyze-Tool/tree/main>
- [13] M. Antivachis, N. Kleynhans, and J. W. Kolar, "Three-phase sinusoidal output buck-boost gan y-inverter for advanced variable speed ac drives," *IEEE Journal of Emerging and Selected Topics in Power Electronics*, vol. 10, DOI 10.1109/JESTPE.2020.3026742, no. 3, pp. 3459–3476, 2022.
- [14] D. Menzi, A. Yang, S. Chhawchharia, S. Coday, and J. W. Kolar, "Novel three-phase electronic transformer," *IEEE Transactions on Power Electronics*, vol. 39, DOI 10.1109/TPEL.2024.3366752, no. 5, pp. 5027–5033, 2024.
- [15] M. Zhang, J. Tong, Z. Chen, and A. Q. Huang, "A unified numerical modeling method for dual active bridge type converter," in *2023 IEEE Energy Conversion Congress and Exposition (ECCE)*, DOI 10.1109/ECCE53617.2023.10362268, pp. 3035–3041, 2023.
- [16] F. Krismer and J. W. Kolar, "Closed form solution for minimum conduction loss modulation of dab converters," *IEEE Transactions on Power Electronics*, vol. 27, DOI 10.1109/TPEL.2011.2157976, no. 1, pp. 174–188, 2012.
- [17] R. Baranwal, K. V. Iyer, K. Basu, G. F. Castellino, and N. Mohan, "A reduced switch count single-stage three-phase bidirectional rectifier with high-frequency isolation," *IEEE Transactions on Power Electronics*, vol. 33, DOI 10.1109/TPEL.2018.2790800, no. 11, pp. 9520–9541, 2018.
- [18] L. Shu, W. Chen, M. Shi, R. Liu, S. Gao, and F. Deng, "Improved control strategy of triple-voltage three-phase dab (t2-dab) converter for current stress and zero-voltage-switching optimization," *IEEE Journal of Emerging and Selected Topics in Power Electronics*, vol. 10, DOI 10.1109/JESTPE.2021.3060477, no. 1, pp. 773–784, 2022.
- [19] S. S. Muthuraj, V. K. Kanakesh, P. Das, and S. K. Panda, "Triple phase shift control of an ill tank based bidirectional dual active bridge converter," *IEEE Transactions on Power Electronics*, vol. 32, DOI 10.1109/TPEL.2016.2637506, no. 10, pp. 8035–8053, 2017.



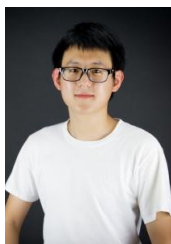
Mafu Zhang received the B.S. degree in electrical engineering and automation, from Xi'an Jiaotong University, Xi'an, China, in 2017, the M.Sc. degree in energy science and technology from ETH Zürich, Zürich, Switzerland, in 2021. He is currently working toward the Ph.D. degree with the Semiconductor Power Electronics Center (SPEC), The University of Texas at Austin, Austin, TX, USA.



Huanghaohe Zou received the B.S. degree in electrical engineering from Xi'an Jiaotong University, Xi'an, China, in 2019. He is currently working toward the Ph.D. degree in electrical and computer engineering with the University of Texas at Austin, Austin, TX, USA.



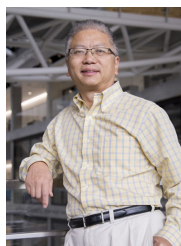
Saleh Farzamkia received the B.S. degree (with Hons.) from Bu-Ali Sina University, Hamedan, Iran, in 2013, and the M.Sc. degree (with Hons.) from the University of Tehran, Tehran, Iran, in 2015, both in electrical engineering. He is currently working toward the Ph.D. degree with The University of Texas at Austin, Austin, TX, USA.



Zibo Chen received the B.S. degree from the Dalian University of Technology, Dalian, China, in 2016, and the M.Sc. degree from the Huazhong University of Science and Technology, Wuhan, China, in 2019, all in electrical engineering. He is currently working toward the Ph.D. degree with the University of Texas at Austin, Austin, TX, USA.



Chen Chen received the B. S. degree from the Harbin Institute of Technology in electrical and automation engineering in 2020. He is currently working toward the Ph.D. degree with the University of Texas at Austin, Austin, Tx, USA.



Alex, Q. Huang (Fellow, IEEE) received the B.Sc. degree in electrical engineering from Zhejiang University, Hangzhou, China, in 1983, the M.Sc. degree in electrical engineering from the Chengdu Institute of Radio Engineering, Chengdu, China, in 1986, and the Ph.D. degree from Cambridge University, Cambridge, U.K., in 1992. He is the Dual D. Cockrell Centennial Chair in Engineering and the director of the Semiconductor Power Electronics Center at the University of Texas at Austin.